Uncertainty of Radiometer Calibration Loads and Its Impact on Radiometric Measurements

Matti Kaisti, Miikka Altti, and Torsti Poutanen

***Abstract*—We present an uncertainty analysis of radiometer calibration. The procedure can be used to determine the uncertainty in the nominal brightness temperature of the unknown scene. Total power radiometer requires frequent calibration with known reference loads that are connected to the radiometer. Our analysis includes uncertainties from the radiometer calibration loads and from the connecting network that is required to multiplex calibration loads and scene to the radiometer input. We show the design and analysis of three calibration loads and how their uncertainties propagate from load terminals to the radiometer calibration plane and to the scene. All three loads, including a cryogenic load, are simple, inexpensive and show great stability and accuracy. We give an uncertainty calculation example for our three calibration loads and for the connecting network. We validate our model and the long term stability of the loads through measurements. The analysis is done at 52 GHz, but the analysis and the construction of the loads are generic and easily scalable to other frequencies.**

***Keywords*—calibration, cryogenic load, radiometers, remote sensing**

I. Introduction

RADIOMETERS have been used in remote sensing to measure various properties related to the atmosphere and surface of the Earth. Radiometers require calibration to relate radiometer output voltage to the input brightness temperature. Square law power detectors are commonly used to relate the output DC voltage linearly to the input power. If a linear radiometer transfer function is assumed, a minimum of two input noise references are needed to calibrate a total power radiometer. The uncertainty of the calibration is mainly determined by the uncertainty of the used calibration references and by the uncertainty in the scattering parameters of the network that connects different loads to the radiometer.

For good radiometric resolution, it is required to have the brightness temperature of one of the calibration loads close to the brightness temperature of the scene. Commonly viewed scenes have low emissivities or physical temperatures leading to low scene brightness temperatures. Therefore substantial effort has been given to construct cryogenic loads [1]–[4]. These loads are either high performance, simple or inexpensive, but none combine all these features with a detailed uncertainty analysis. We present a cryogenic load that is simple, inexpensive and accurate. We do not only model our cryogenic load but also measure it.

The connecting network between the radiometer input and the calibration loads or scene changes the brightness temperature when a signal travels through it. This is due to the losses of the connecting network and reflections in the signal path. By knowing these characteristics their effect can be removed but the limit by which they are known creates uncertainty in radiometer calibration. We report for the first time a full analysis of the total power radiometer calibration uncertainty. For this it is required that both (or all) used calibration load uncertainties and the uncertainty in the connecting network are included when the final uncertainty in the scene brightness temperature is measured.

This paper is organized as follows: in the Section II we establish the required definitions and describe the problem to which we propose a solution. In Sections III through V we show how the nominal brightness temperatures of our calibration loads with corresponding uncertainties at 52 GHz are obtained. The cryogenic load is far more complex than the other two and therefore a large portion of this paper is devoted to its analysis. In Section VI we describe how the connecting network between the loads and the radiometer changes the load brightness temperatures and what is the related uncertainty. In the Section VII we verify our analysis and the final section concludes the paper.

II. Preliminaries

A. Temperature Definitions

In this paper three different temperature quantities are used: *physical temperature* (T_{phys}), *Rayleigh-Jeans temperature* (T_{RJ}) and *brightness temperature* (T_B).

The physical temperature of an object is the temperature that can be measured at its surface using a thermometer. We call Rayleigh-Jeans (RJ) temperature the temperature that is related to the radiation from a blackbody, which results from its physical temperature as

$$T_{RJ} = \frac{x}{e^x - 1} T_{phys} \tag{1}$$

where $x = hf/kT_{phys}$, h is the Planck constant, f is the frequency and k is the Boltzmann constant. Brightness temperature of an object is related to the power spectral density (N) per mode that it emits as $N = kT_B$. The brightness temperature of a real object is $T_B = eT_{RJ}$ where e is the

Manuscript received February 19, 2014; revised May 27, 2014.

M. Kaisti was with DA-Design OY, Keskuskatu 29, FI-31600 Jokioinen, Finland. He is now with the the Technology Research Center, University of Turku, 20014 Turun Yliopisto, Finland, e-mail: matti.kaisti@utu.fi

Miikka Altti is with DA-Design OY, Keskuskatu 29, FI-31600 Jokioinen, Finland, e-mail: miikka.altti@da-design.fi

Torsti Poutanen was with DA-Design OY, Keskuskatu 29, FI-31600 Jokioinen, Finland. He is now with Elektrobit Wireless Communications Ltd, Tutkijantie 8, FI-90590 Oulu, Finland. email: torsti.poutanen@kolumbus.fi

emissivity of the object surface. It is one for a blackbody, but for any real object it lies between zero and one. [5]

B. Problem Description

A lot of attention has been given to analyzing radiometric resolution. What has been neglected is the uncertainty in the scene nominal brightness temperature. Figure 1 presents a simplified block diagram of a radiometer measurement setup is presented. A radiometer is connected to three loads through a connecting network. Two loads are required to calibrate a radiometer. The third connected load would generally be the scene that is being measured. In our analysis we connect three calibration loads to the three radiometer ports. These loads are the calibration loads which we designed and constructed, the Cryogenic load (CL), the Ambient temperature load (AL) and the Heatable load (HL). The Cryogenic load has an absorber cooled down to liquid nitrogen boiling point, the Ambient temperature load is a waveguide termination close to the room temperature and the Heatable load is a waveguide termination that can be heated up to 80 C. For their nominal brightness temperatures we use symbols T_{CL}, T_{AL} and T_{HL}. We also use a common symbol T_{RL} for these reference loads.

The connecting network (CN) provides a signal path from a load to the radiometer. A connecting network comprises passive microwave components and it is characterized by a scattering matrix. It has the ability to multiplex one load to the radiometer input from a set of three. This is achieved by two waveguide switches. This path in terms of losses and reflections is different for each load and thus all loads need to be referenced to a common calibration plane. The conversion from a load to calibration plane we call the *Forward Conversion*. It removes load specific effects in each signal path.

In the calibration plane the radiometer gain and offset term are solved using the converted calibration load brightness temperatures. With the calibrated radiometer the measured scene brightness temperature can be solved at the calibration plane. This brightness temperature is then converted back to the plane of the scene which is the solved brightness temperature of the scene. We call this conversion the *Reverse conversion*. The steps described above each contain some uncertainty in them. What is the net effect of all of these steps to the total uncertainty in the solved scene brightness temperature is not known.

C. Method

To solve the described problem we constructed a simulation model that is based on both theoretical calculations and vector network analyzer (VNA) measurements. Our model can be summarized with the following steps:

1) Compute nominal values and uncertainties of the reference load brightness temperatures T_{RL}.
2) Convert T_{RL} with uncertainties from step 1 to the calibration plane and add CN uncertainties. This is the *Forward Conversion*.

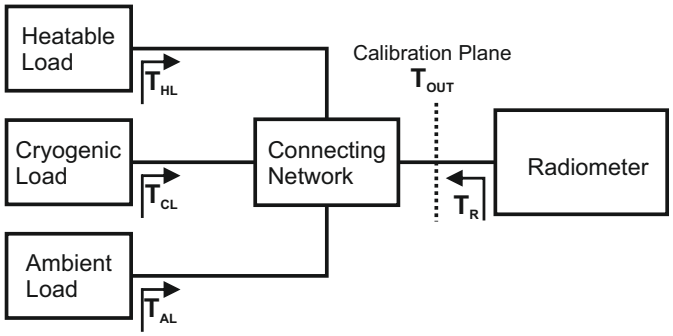

Fig. 1. Simplified block diagram of a radiometer measurement setup. The reference loads emit noise towards radiometer through the Connecting Network at brightness temperatures T_{HL}, T_{CL} and T_{AL}. The brightness temperature T_R is effective noise fed towards the reference loads from the radiometer port. T_{OUT} is the brightness temperature at the Calibration Plane.

3) Calibrate the radiometer with the reference load brightness temperatures i.e. determine the radiometer gain and offset.
4) Solve for the scene brightness temperature at the calibration plane.
5) Convert the scene brightness temperature from the Calibration Plane to the scene and add the CN uncertainties. This is the *Reverse Conversion*.

The uncertainties in each step relate to each other consecutively and to account each effect we built a Monte Carlo Simulation (MCS). Our model accounts the uncertainties of each calibration load and both conversions. Each load contain some uncertainty in its nominal brightness temperature. The Cryogenic load uncertainty analysis is complex and therefore we used a MCS to compute its brightness temperature uncertainty. The Ambient load uncertainty analysis is simple and since it equals the uncertainty of the underlying physical temperature measurement. The Heatable load uncertainty is dominated by the physical temperature measurement uncertainty, but since it is a heated load there is a physical temperature gradient in the waveguide that connects it to the radiometer. To account all effects in its brightness temperature, a MCS is used. The Monte Carloed streams at load terminals serve as an input to the connecting network Forward Conversions. In this conversion we add the uncertainties of the connecting network using MCS. At this point a stream of scene brightness temperatures can be solved for at the calibration plane. Finally this stream is converted back to the scene terminals where additional uncertainties are added from the connecting network. This stream finally reveals the uncertainty by which the scene brightness temperature can be solved.

III. Cryogenic Load

A. Construction

The two common methods of creating a cryogenic load with liquid nitrogen (LN2) are to submerge a matched load in liquid nitrogen [1] and to view a cooled absorber with an antenna connected to the radiometer [2]–[4].

At millimeter wave frequencies the submerged termination alternative, the loss of the transmission line, commonly a waveguide that connects the radiometer input to a matched load, creates uncertainty in the load brightness temperature not easily circumvented [3]. For lower frequencies such transmission line based solution has proved useful [6]. The waveguide losses and the temperature profile along the waveguide have to be known with great accuracy. Heat flow from warm ambient to the cooled load creates uncertainty to the physical temperature of the load. Dry nitrogen would have to be blown in the waveguide to prevent icing inside the waveguide. The physical temperature is also difficult to measure since the actual absorber material is inside a waveguide.

A more practical approach can be achieved by cooling an absorber material with LN2 and using an antenna connected to the radiometer to view the cooled absorber. A mechanical drawing of our Cryogenic load is shown in Fig. 2. A radiometer is placed directly beneath a polystyrene box. An antenna connected to the radiometer input views a cooled absorber placed at the bottom of the box through the polystyrene box base. Observing the load though the box base creates a stable operating condition compared to a construction where the absorber is viewed from above. As the LN2 boils, its level decreases which leads to an oscillation in the measured brightness temperature due to the changing reflection at the air-LN2 interface. For example, in [7] an oscillation amplitude up to 1.5 K is observed. Furthermore, our approach ensures very long cold periods. With a practical tank size several hours can be easily achieved with one filling which can be easily extended by just pouring more LN2 into the tank without any effect on the load brightness temperature.

The reflection resulting from air-polystyrene foam is small since the polystyrene foam has dielectric constant close to unity. This, however, is susceptible to change if the polystyrene base temperature drops below dew point and water condenses on the surface. This is prevented by blowing a high volume of air along the base surface keeping the temperature of the base at an ambient temperature.

The absorber needs to be secured firmly to the bottom of the polystyrene box to avoid reflection from polystyrene-LN2 interface and to only have polystyrene-absorber interface. For this reason an aluminum plate is placed on top of the absorber to press the absorber tightly against the polystyrene. The absorber needs to be porous and soaked in LN2. An impedance tapered flat absorber with return loss better than 30 dB, measured by the manufacturer, was chosen. The used absorber was Eccosorb HR-25 provided by Emerson & Cuming. An interface between free space and a very lossy medium has a high impedance discontinuity and therefore will act as a reflector. By engineering the front of the absorber with dielectric properties close to that of free space, reflections can be minimized. Our configuration uses several layers of the mentioned absorber in back-to-back configuration so that there is no impedance discontinuity between the absorber sheets. This should also slightly improve the return loss compared to single sheet since now the reflections from the sheet back interface can be neglegted.

To ensure that only small amount of thermal noise is picked by the antenna side and back lobes a low emissivity cavity is constructed around the antenna. A polished copper coated cavity is placed around the antenna so that the antenna sees only this low emissivity material with its side and back lobes and the cooled absorber with its main beam. The cross-section of the cavity is a square with rounded corners. Rounding the corners prevents unwanted resonances from occurring [3]. We envision that by having strictly cylindar shaped cavity as shown in Fig. 2, the design is further improved.

The resulting brightness temperature of the designed Cryogenic load is close to the LN2 boiling point, but it is slightly increased due to polystyrene box dielectric losses, antenna side and back lobe contribution and antenna losses.

We discuss these effects individually. However, these effects are related to each other in consecutive steps where the output of a previous step serves as an input to the next. We used a MCS to compute the Cryogenic load brightness temperature and its uncertainty. The steps to solve the Cryogenic load brightness temperature are

1) Compute LN2 boiling point (T_{LN2}).
2) Compute the brightness temperature of the bottom surface of the polystyrene box (T_{PS}).
3) Compute the effective brightness temperature seen by the antenna (T_A).
4) Compute the brightness temperature at the antenna terminal (T_{CL}). This is the brightness temperature seen at the Cryogenic load terminal.

B. Liquid Nitrogen Boiling Point

The absorber in the LN2 tank is assumed to be perfectly non-reflecting and therefore the absorber brightness temperature equals the LN2 boiling point. The boiling point of the liquid nitrogen depends on the atmospheric pressure. A model relating atmospheric pressure to the LN2 boiling point is given in [8]

$$T_{LN2}^{phys} = T_C + C\Delta P \tag{2}$$

Here $T_C = 77.36$ K is the LN2 boiling point at the reference pressure of $P = 1013.25$ hPa. The factor C is a constant, whose value is $C = 0.0082409$ K/hPa. ΔP is the pressure difference from the reference pressure. The RJ temperature of LN2 boiling point can be calculated with Eq. (1). Other models for LN2 boiling point are given in [9]. However, with naturally occurring atmospheric pressures the differences between the models are negligible.

We measured the air pressure of the lab with an accuracy of $\pm$ 0.3 hPa. In [8] no uncertainty to coefficients T_C or C are given. Without better information we assume that they are precise.

The LN2 boiling point is only strictly valid at the top surface. There is an increase in the total pressure at the bottom of the box due to hydrostatic pressure. This pressure increase also increases the observed LN2 brightness temperature. The hydrostatic pressure is $\rho g h$ where ρ is the LN2 density, g is

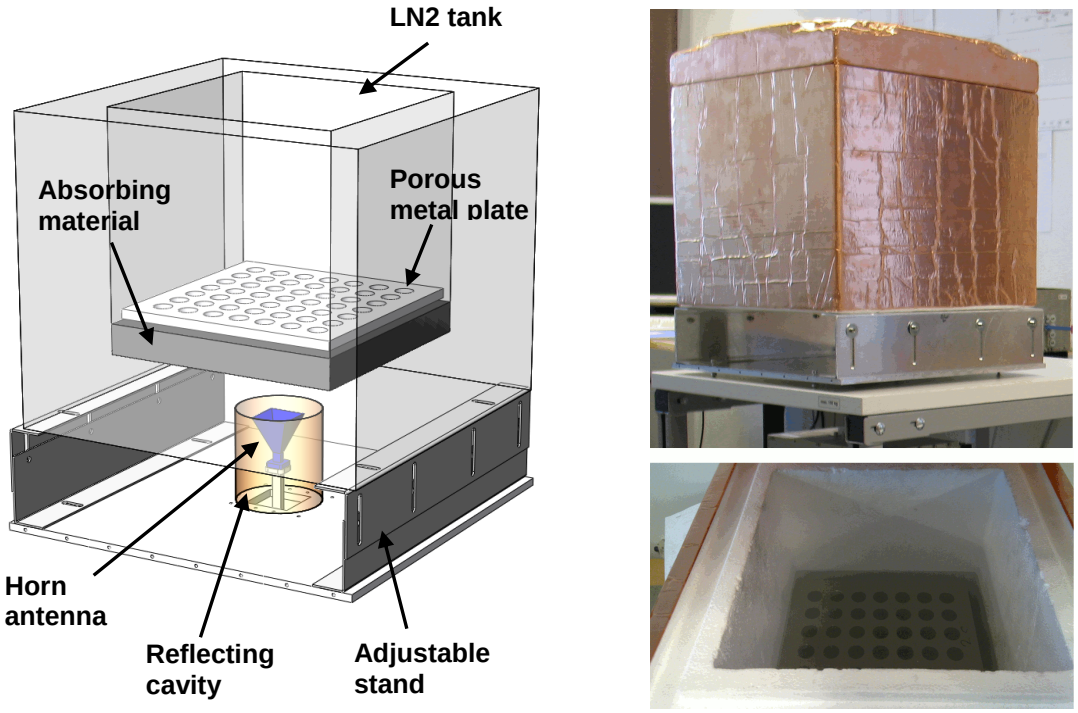

Fig. 2. a) Illustration of the Cryogenic load. The LN2 tank (polystyrene box) is shown as transparent. The polystyrene base of the tank is between the horn antenna and the absorbing material. b) Constructed Cryogenic load. Top: The Cryogenic load is covered with copper tape to shield it from ambient noise. Bottom: Cryogenic load with cover removed and LN2 poured into the tank.

the gravity of Earth and h is the height of the liquid column above the absorber observation plane. The maximum used h was 8 cm and the density of LN2 is 808 kg/m^3. This results in 6.3 hPa pressure increase at the box bottom compared to the LN2 surface. According to the model this results in a 0.05 K boiling point increase at the bottom. This difference in the boiling points decrease when the LN2 boils due to falling liquid column height. The hydrostatic pressure with common LN2 cooldowns produce negligible error compared to the dominant error sources of the design. Therefore we omit it from our analysis.

C. Brightness Temperature of the Polystyrene Base

The polystyrene foam has dielectric constant close to unity. Therefore the reflection resulting from air-polystyrene foam interface is small and its effect on the Cryogenic load brightness temperature is small. Reported values for dielectric constants for polystyrene foam range from measured values of 1.017 to 1.022 in frequency range of 0.2 to 4 THz with only little variation in frequency [10]. Empirically derived formula for scaling the dielectric constant of a polystyrene and polyethylene resins to their corresponding foam dielectric constants [11] has been evaluated to yield a dielectric constant of 1.03 at millimeter wave frequencies [4].The power reflection at the interface can be evaluated from the material dielectric constants [12] as $R^2 = |(\sqrt{\epsilon_{air}} - \sqrt{\epsilon_{rf}})/(\sqrt{\epsilon_{air}} + \sqrt{\epsilon_{rf}})|^2$ where ϵ_{rf} is the foam dielectric constant.

The brightness temperature difference between the LN2 and the reflecting interface at room temperature is approximately 220 K. This leads to a worst case increase of 0.012 K in the brightness temperature when the power reflection is evaluated with polystyrene foam dielectric constant of 1.03. This is worst case since not all noise reflected at the interface is returned to the antenna as the antenna emitted noise diverges upon propagation. This further reduces the amount of reflected noise picked up by the antenna.

Another reflecting interface is found between the polystyrene foam base and the absorber. The polystyrene foam base is practically a dielectric slab with two interfaces and in this system there are infinite amount of reflections and refractions. Depending on the box bottom thickness the reflections from the two interfaces can add either constructively or destructively. In the worst case the total return loss is close to 30 dB. There is a fair gap between the antenna and the absorber. The gap comprises from the small air gap between the antenna and polystyrene foam box bottom and from the polystyrene foam base thickness. As noise emitted by the antenna propagates this gap it is quite strongly diverged depending on the antenna directivity. Therefore most of the noise emitted by the antenna and reflected from the interface is not returned to the antenna. A highly conservative worst case analysis leads to 0.22 K error in the calculated brightness temperature. We envision that the error is much smaller than the worst case analysis and therefore we omit it from the analysis.

However, it has to be noted that if the antenna emitting noise is significantly greater than the one emitted by an isolator at room temperature, the induced error would also significantly increase. In situations where the effect cannot be ignored a detailed analysis describing the difference in the antenna reflection when near by targets are compared to distant scenes is given in [13].

Polystyrene foam and polyethylene foam are both promising candidates for the presented application due to their suitable microwave properties. The latter produces approximately one order in magnitude smaller radiometric error than polystryrene foam. [14] By replacing the polystyrene foam box with polyethylene foam box we believe that the effect of the box base loss (which we discuss later) and reflections from air-box base (which we omit) could be safely ignored even at higher frequencies.

The polystyrene foam box base effectively increases the brightness temperature at the bottom surface of the box since the antenna views the absorber through this dielectric base. The increase depends on the box base physical temperature and its dielectric losses.

The polystyrene box base physical temperature is not constant. Inside the box (where the LN2 is poured) the base top surface is at LN2 boiling point. The box bottom surface is near the ambient temperature of the room, but decreased due to LN2 cooling it. We assume that there is linear temperature gradient between the two surfaces.

Polystyrene foam is a mixture of polystyrene resin and air. The real part of the dielectric constant of such a mixture is given in [11]

$$\epsilon_{rf} = \frac{2}{5}\epsilon_{r0}^{d_f/d_0} + \frac{3}{5}\left[1 + \frac{d_f}{d_0}(\epsilon_{r0} - 1)\right] \tag{3}$$

where ϵ_{r0} is the real part of the dielectric constant of the polystyrene resin, d_0 is the density of the polystyrene resin and d_f is the polystyrene foam density. The loss tangent of the polystyrene resin is given by the empirical formula [4]

$$tan\delta_0 = 0.89 \times 10^{-3} + 6.01 \times 10^{-6} f \tag{4}$$

where f is the frequency in GHz.

The imaginary part of the dielectric constant of the polystyrene resin is assumed to scale linearly with density when the foam is formed [4]. Therefore the loss tangent of the foam is

$$tan\delta_f = \frac{d_f}{d_0}\frac{\epsilon_{r0}}{\epsilon_{rf}} tan\delta_0 \tag{5}$$

The dielectric loss coefficient of the polystyrene base (for TEM mode) is given by [15]

$$\alpha_d = \frac{\pi\sqrt{\epsilon_{rf}} \times tan\delta_f}{c} f \tag{6}$$

where c is the speed of light. The loss in dB/m is obtained by multiplying α_d by $20log(e)$.

The brightness temperature at the bottom surface of the polystyrene box is calculated by dividing the base to N-1 thin slices of constant physical temperature. T_{base}^n is the RJ temperature of the nth slice. The RJ temperature of the first slice is the RJ temperature of the LN2 boiling point T_{LN2} and the T_{C0} is the RJ temperature of the last slice. T_{C0} is also the common RJ temperature of the antenna, cavity wall and the bottom surface of the box. The brightness temperature from each slice is the input to the next slice and this way the final output brightness temperature (T_{PS}) is obtained recursively from

$$T_{PS}^{n+1} = gT_{PS}^n + (1-g)T_{base}^{n+1} \tag{7}$$

where $T_{PS}^1 = T_{LN2}$, $T_{base}^1 = T_{LN2}$ and $T_{base}^N = T_{C0}$, g is the loss factor of the slice: $g = 10^{-L/(10N)}$. L is the total attenuation of the base in dB. We repeated the recursive computation of T_{PS} and increased the number of slices for each repetition until the value of T_{PS} no longer changed. We found N = 1000 to be sufficient for the computation of T_{PS}.

The values used for the polystyrene resin and density were $\epsilon_{r0} = 2.54$ and $d_0 = 1050$ kg/m^3 respectively [11]. Our box had a polystyrene foam density of $d_f = 27.8$ kg/m^3.

Uncertainties used in the MCS were the thickness variation of the base and the RJ temperature of the bottom surface of the LN2 box. The nominal thickness of box base was 3.3 cm with an uncertainty of 0.25 cm. Due to a thermal leak through the bottom of the box, the bottom surface temperature is slightly decreased from the ambient temperature. The box bottom temperature profile was determined by measuring the bottom at several points. These measurement readings differed negligibly. We used the physical temperature of the Cryogenic load antenna, which we measure, as the physical temperature of the bottom and added a conservative uncertainty of -30. . .0 K to it. Uncertainties associated with the model of the base loss [4] are unknown and without better information we assume it to be precise.

D. Apparent Antenna Temperature

There are two sources of photons that enter the antenna of the Cryogenic load. Firstly there are photons that enter the antenna directly from the cold bottom surface of the polystyrene box. Secondly there are photons that have been reflected from the cavity walls. The bottom surface of the box is at the brightness temperature T_{PS} (computed in the previous section), whereas the rest of the antenna surroundings has a higher brightness temperature. We call this wall brightness temperature T_{wall}.

The apparent antenna temperature (T_A) seen by the antenna is the brightness temperature field convolved with the antenna power pattern. This gives the brightness temperature of the load seen with a lossless antenna. The convolution is computed over the full spherical surface. The antenna power pattern $G(\theta, \phi)$ and the brightness temperature field $T(\theta, \phi)$ are both functions of spherical angles and the apparent antenna brightness temperature is given by [5]

$$T_A = \frac{\int_{4\pi} G(\theta,\phi)T(\theta,\phi)d\Omega}{\int_{4\pi} G(\theta,\phi)d\Omega} \tag{8}$$

The cavity walls were coated with copper tape for low emissivity. In a simple single reflection model a photon emitted by the cold surface is first reflected from the cavity wall before absorbed by the antenna. The brightness temperature in such case can be calculated as

$$T_{wall} = eT_{C0} + (1-e)T_{PS} \tag{9}$$

where e is the emissivity of the cavity wall.

In reality the photons may experience a large number of reflections before entering the antenna. The cold bottom surface of the polystyrene box both emits photons into the cavity and absorbs photons from it. The probability of absorption p is assumed to be the ratio of the surface area of the photon absorbing surface of the cavity to its total area. In this model the brightness temperature after the nth reflection can be computed with the following converging recursive relation

$$T^n_{wall} = pT_{PS} + (1-p)\left[eT_{C0} + (1-e)T^{n-1}_{wall}\right] \tag{10}$$

The antenna is placed close to the bottom surface of the polystyrene box to ensure that the absorber covers fully the antenna main beam. This leads the bottom of the Cryogenic load being in the near-field. Antenna patterns have been simulated with high frequency structural simulator (HFSS) near-field simulation. The load the antenna is viewing is the flat bottom surface of the box, which results in the cavity corners being further apart from the antenna than the point directly above the antenna. Two near field simulations with these two extreme distances were carried out. The antenna beam gets narrower with smaller distances. In these cases the cavity wall contribution gets smaller and therefore the apparent antenna temperature is reduced as compared to the larger near-field distances.

There is a certain amount of uncertainty in the antenna pattern, because the distance from the antenna phase center to the bottom surface of the polystyrene foam box varies with elevation angle. We considered the two near-field patterns computed above as the extremes of the pattern uncertainty, and swapped randomly between them in the MCS that we used in computing the uncertainty of the antenna apparent temperature.

From the simulations it is found that to keep the side and back lobe contributions low, the antenna should be placed as close as possible to the polystyrene box base surface. A small air gap has to be left to let the air flow freely over the base surface to avoid condensation. The effect of antenna back and side lobe contribution is minimized with high-reflectivity cavity surface material. Polished copper tape is placed at the surface to cover all sides of the cavity except the opening where the cold absorber is viewed. We used emissivity range of 0.0025. . .0.05 for the copper. The lowest value is given to polished copper and the highest for tarnished copper. The cavity wall temperature cool downs due to the thermal leak of the box bottom. In operational use a maximum measured deviation in the wall temperature was 5 K. We therefore assigned an uncertainty of 0. . .-5 K to it. The cavity wall temperature calculation was presented in two ways and we randomly swapped between the two. Additionally the antenna vertical position was assigned a ± 1 cm uncertainty. This fairly high uncertainty includes small variations in the box bottom thickness as well as the uncertainty in determining the actual position of the antenna phase center. The vertical movement changes the brightness temperature field seen by the antenna. However, the design is quite insensitive to this variation as long as the antenna main beam only sees the cold absorber and not the warmer cavity surfaces.

E. Brightness Temperature at the Antenna Terminal

The antenna loss affects the brightness temperature of the noise that comes out from the antenna. The antenna loss for waveguide horn antennas can be calculated using waveguide attenuation theory. The antenna shape profile is modelled as a waveguide where the flare section is considered as a waveguide with increasing dimensions. Slicing this profile in the antenna axis direction and calculating the attenuation in each slice and integrating over the profile leads to the total attenuation of the antenna. [3] The following discussion applies to rectangular waveguides.

The unitless power attenuation of a rectangular horn antenna is calculated using

$$\alpha = e^{2K\int \alpha_c dz} \tag{11}$$

where K is a surface roughness factor and α_c is the conductor loss in Np/m and the integration is performed from 0 to z where z is the antenna length. For air-filled waveguide the dielectric losses can be neglegted. For a standard rectangular waveguide the width a is greater than the height b and hence the dominant mode is TE_{10} and the cutoff frequency is $f_c = c/2a$. The conductor losses for TE_{10} mode can be calculated with [15]

$$\alpha_c = \frac{R_S}{\eta b}\frac{\left(1+\frac{2bf_c^2}{af^2}\right)}{\sqrt{1-\frac{f_c^2}{f^2}}} \tag{12}$$

where f_c is the waveguide cutoff frequency, f is the frequency and wave impedance $\eta = \sqrt{\mu/\epsilon}$, where ϵ and μ are the free space (for air-filled waveguide) permittivity and permeability respectively. R_S is the surface resistance of the conductor, which is given by

$$R_S = \sqrt{\frac{\omega\mu}{2\sigma}} \tag{13}$$

where $\omega = 2\pi f$ and σ is the conductivity of the waveguide inner wall. Its thickness is assumed to be several skin depths. The antenna is connected to the radiometer with a piece of rectangular waveguide. This ensures that no modes other than TE_{10} can propagate.

The surface roughness factor K was obtained by a measurement. The attenuation of waveguide (made from the same material from which the antennas were manufactured) was measured and compared to the theoretical loss of a perfectly smooth waveguide with the same material conductivity. This comparison revealed the values for K. Especially for higher frequencies, the surface roughness is believed to be the

dominant factor increasing waveguide loss above that for a perfectly smooth waveguide. Even if other factors contribute, they are included since the K factor values were obtained from measurements. We found that K = 1.04 for our antenna and the calculated antenna power attenuation including the waveguide that connects the antenna to the connecting network is 0.123 dB. The final noise temperature of the Cryogenic load seen at the antenna terminal can be calculated with [3]

$$T_{CL} = \eta_l T_A + (1 - \eta_l) T_{C0} \tag{14}$$

where $\eta_l = 1/\alpha$. The antenna physical temperature was measured with a class A platinum sensor with a ± 0.3 K uncertainty. Antenna material conductivity was assigned a $\pm 20\%$ uncertainty. The antenna is connected to the radiometer with a short waveguide. We assumed ± 0.1 mm uncertainty in all dimensions of the antenna and the waveguide.

F. Brightness Temperature Uncertainty

The brightness temperature of the Cryogenic load was computed from the model that we described above. MCS was made to account for the uncertainties in the model parameters. The parameters and their uncertainties were described above. In the MCS the parameters were varied uniformly within their uncertainty ranges. Antenna pattern and cavity wall temperature had only two possible values. In these cases we let the simulation to randomly choose from the two possibilities.

The brightness temperature obtained is shown in Fig. 3. These curves are the brightness temperature outputs from the four steps we described. Each previous step serves as an input to the next. The baseline is given by the bottom curve (black) which is the RJ temperature of the LN2 boiling point. The uncertainty in it is small since the atmospheric pressure measurement is accurate and the sensitivity of the LN2 boiling point to atmospheric pressure is low. The brightness temperature and uncertainty increases in the second curve (green) are small since the polystyrene box loss is small. The increase from T_{PS} to T_A, the third curve (red), is modest because the antenna has fairly high directivity and the antenna main beam views mainly the cooled part of the Cryogenic load and not so much the warmer cavity walls. This could be easily improved by using e.g., a corrugated horn antenna with lower side- and backlobe contributions. The impact of the final step, the top curve (blue), to the Cryogenic load brightness temperature is more significant than the previous steps. This shows clearly that the total resistive loss of the antenna and the waveguide that connects the antenna to the radiometer dominates the Cryogenic load brightness temperature increase and its uncertainty. The loss (in dB/m) is highest within the waveguide part having small dimensions compared to the flare section with larger dimensions. Removing this part or making it very short would reduce the significance of this step. The predicted Cryogenic load uncertainty approaches a normal distribution and the uncertainty is given in standard deviations in Fig. 3.

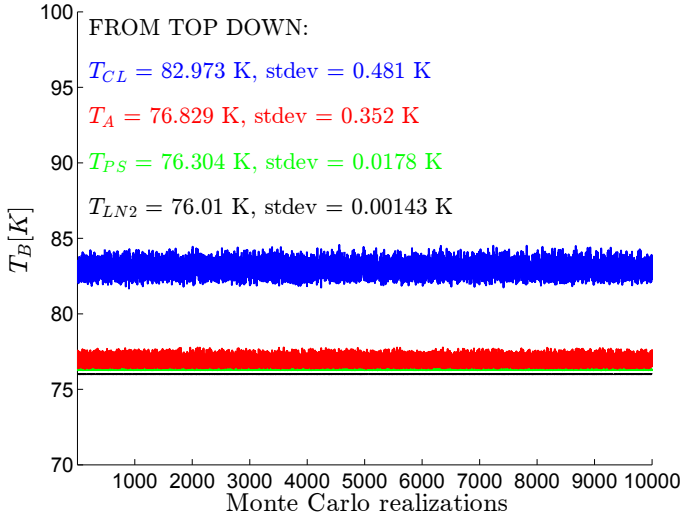

Fig. 3. Cryogenic load brightness temperature uncertainty simulation for 52 GHz.

IV. Ambient Temperature Load

Radiometers require temperature stabilization for accurate and stable measurements. We used a Peltier element to keep the thermally insulated radiometer housing at a constant temperature. The Ambient temperature load that we use as a calibration load is enclosed in this housing. The brightness temperature of the Ambient temperature load is directly measured from its terminals. There are no added lossy connecting components and the used load has return loss better than 30 dB. Therefore its brightness temperature equals its RJ temperature. We monitor its physical temperature with a class A PT1000 sensor. This information can be used to solve its RJ temperature using Eq. (1) which equals its brightness temperature T_{AL}. Therefore the uncertainty of T_{AL} is determined by the underlying physical temperature measurement. The temperature measurement uncertainty with the used platinum sensors is ± 0.3 K.

V. Heatable Load

The Heatable load comprises a Peltier element, Peltier controller, heat sink, insulated enclosure, stainless steel waveguide, waveguide termination and a copper waveguide that connects the Heatable load to the radiometer. The physical temperature of the waveguide termination can be adjusted using the Peltier control. The construction of the load is shown in Fig. 4. The Peltier element is placed beneath the termination. Thermally insulating material is placed adjacent to the outer walls of the enclosure, but it is not shown in the Fig. 4 for simplicity. The temperature-controlled waveguide termination is connected to the waveguide interface of the load with two waveguides. The first waveguide is a gold plated thin walled stainless steel waveguide that has a high thermal resistance. One end of the waveguide is at the controlled temperature and the other end is at the ambient temperature. Stainless steel material minimizes the heat flow through the waveguide and keeps the other end of the waveguide at the ambient temperature. The second

waveguide is made from copper and its purpose is to connect the load to the radiometer input terminal. It is entirely at the ambient temperature.

A temperature control range of $0\ldots+90°$C was achieved. The maximum operation temperature of the waveguide termination limits the maximum temperature. The lower limit results from the icing of water vapour inside the waveguide termination creating uncertainty in its RJ temperature. The physical temperature of the waveguide termination is monitored which is used to determine its RJ temperature.

The effect of the temperature profile of the stainless steel waveguide on the load brightness temperature was investigated. The brightness temperature was computed in two ways. We assumed a linear temperature gradient in the waveguide or we assumed simply that the entire waveguide is in the average of the temperatures of the waveguide ends. The brightness temperatures of these two methods differed negligibly. For simplicity we chose the latter approach for the remaining of this work. The brightness temperature of HL is then [12]

$$T_{HL} = T_{TERM}10^{-L/10} + (1 - 10^{-L/10})T_0 \qquad (15)$$

where T_{TERM} is the RJ temperature of the waveguide termination and T_0 is the RJ temperature of the waveguide and L is the loss of the waveguide in dB. The deviation of T_{HL} from its nominal value due to deviations of RJ temperatures and waveguide loss from their nominal values can be computed by differentiating the above equation with respect to T_{TERM}, L and T_0 which results in

$$\Delta T_{HL} = 0.23g(T_0 - T_{TERM})\Delta L + g\Delta T_{TERM} + (1-g)\Delta T_0 \quad (16)$$

where $g = 10^{-L/10}$.

The uncertainty of the first term depends on the accuracy of the waveguide loss measurement. The analysis on this error term is the same as for our Connecting Network measurements and we will complete the discussion of this error term in Section VII. We obtained a value of ± 0.03 K for it.

The uncertainty in both the second and third terms is due to the uncertainty of the underlying temperature measurement which is ± 0.3 K. The loss L of the stainless steel waveguide is close 0 dB and hence g $\approx$ 1. This also means that the second term dominates the total uncertainty. We used a MCS to combine the errors terms of Eq. (16). Uncertainties in all three terms we assumed to be uniformly distributed within the specified ranges. The resulting distribution strongly resembles uniform distribution due to the second error term dominating. The 99% confidence interval estimate for the Heatable load is 0.29 K.

VI. Connecting Network Brightness Temperature Conversions

A reference load is connected to the radiometer input via a lossy two-port connecting network which is characterized by its scattering matrix (this is shown in Fig. 5). The connecting network is inevitably different for each reference load leading to mismatches that introduce error to the measured brightness temperature of the scene if not corrected. A relationship between the brightness temperature of the reference load and radiometer calibration plane can be found by measuring the scattering matrix of the connecting network.

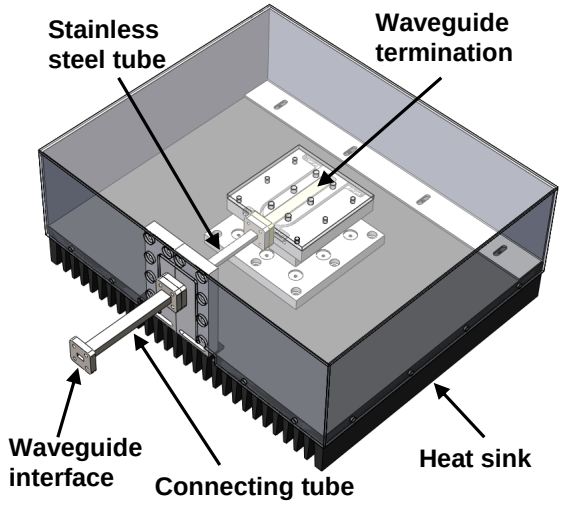

(a)

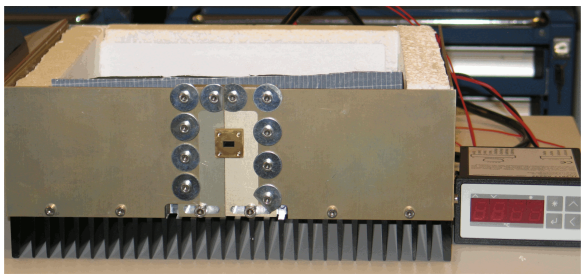

(b)

Fig. 4. a) Illustration of the Heatable Load. The Peltier element (not shown) is between the heat sink and the waveguide termination. The surface of the heat sink as well the load walls and cover are thermally insulated (not shown). b) Constructed Heatable load with top cover opened. Polystyrene thermal insulation is shown adjacent to the outer walls of the enclosure. Peltier controller is seen on the right side of the load.

In a radiometric measurement two conversions are needed. After the reference load temperatures are determined they need to be converted to the calibration plane of the radiometer. These converted temperatures can be used in calibrating the radiometer response. This is called a *Forward Conversion*. When the scene has been solved at the calibration plane it needs to be converted back to the scene interface. This is called the *Reverse Conversion*.

A. Forward Conversion

The following equations are reproduced from [12]. Equation (17) gives the components that contribute to the converted brightness temperature. T_{RL} is the reference load brightness temperature which is a common term for all reference loads. T_0 is the RJ temperature of the connecting network and T_R is the brightness temperature of the effective reverse noise feed of the radiometer (noise fed towards the loads). Our radiometer

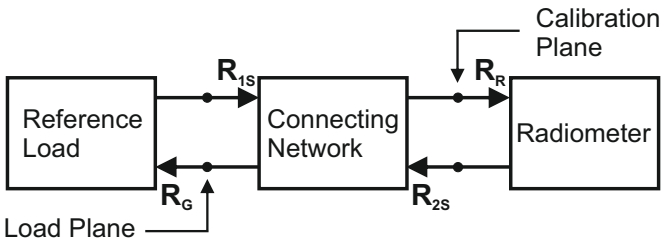

Fig. 5. Connecting Network between radiometer and a calibration reference or an unknown scene. Figure adapted from [12].

has an isolator in its input stage and therefore the reverse noise feed represents the noise of a termination that is placed in the operating temperature of the radiometer. The brightness temperature T_{RL} conversion at plane 1 to T_{OUT} at plane 2 is given by

$$T_{OUT} = \alpha_m \gamma T_{RL} + \alpha(1-\gamma)T_0 + (1-\alpha_m)T_R \qquad (17)$$

where $\alpha_m \gamma T_{RL}$ = net delivered noise from the generator, $\alpha_m(1-\gamma)T_0$ = net delivered noise from the lossy network due to self-emission, and $(1-\alpha_m)T_R$ = net delivered noise from the receiver and then reflected back towards the receiver. The above parameters are given by

$$\alpha_m = \frac{(1-|R_{2S}|^2)(1-|R_R|^2)}{|1-R_{2S}R_R|^2} \qquad (18)$$

and

$$\gamma = \frac{1}{L_S}\left[\frac{(1-|R_G|^2)(1-|S_{11}|^2)}{|1-S_{11}R_G|^2(1-|R_{2S}|^2)}\right] \qquad (19)$$

where $R_{2S} = S_{22} + \frac{S21S_{12}R_G}{1-S11R_G}$ and $L_S = \frac{Z_{02}}{Z_{01}}\frac{(1-|S_{11}|^2)}{|S_{21}|^2}$. R_G and R_R are the voltage reflection coefficients of the noise generator and the radiometer input respectively. Z_{01} and Z_{02} are characteristic impedances at the connecting network ports and they are usually equal. If zero reflections are assumed, Eq. (17) simplifies to

$$T_{OUT} = \gamma T_{RL} + (1-\gamma)T_0 \qquad (20)$$

B. Reverse Conversion

The brightness temperature of the unknown load is given at the Calibration Plane. To determine the brightness temperature of the load itself it needs to converted by

$$T_{RL} = \frac{T_{OUT} - \alpha_m(1-\gamma)T_0 - (1-\alpha_m)T_R}{\alpha_m \gamma} \qquad (21)$$

where the parameters have the same meaning as they did in the Forward Conversion.

TABLE I. CONNECTING NETWORK (CN) AND RADIOMETER PARAMETERS USED IN THE EXPERIMENTAL VERIFICATION.

Parameter	Performance
Radiometer Frequency Band	51.5 ± 2.1 GHz
Radiometer Equivalent Noise Bandwidth	4200 MHz
Radiometer Return Loss	23 dB
CN Heatable Load Return Loss	29 dB
CN Cryogenic Load Return Loss	27 dB
CN Ambient Temperature Load Return Loss	26 dB
CN Heatable Load Insertion Loss	0.4 dB
CN Cryogenic Load Insertion Loss	0.55 dB
CN Ambient Temperature Load Insertion Loss	0.35 dB

C. Brightness Temperature Uncertainties at the Calibration Plane

The uncertainty related to the Forward Conversion depend on the accuracy by which the scattering parameters and RJ temperatures can be determined. The temperature measurements had an uncertainty of ±0.3 K. The scattering parameters uncertainty is determined by the measurement accuracy of the reflections and losses in terms of magnitude and phase. Conversion related parameters including the CN insertion and return losses as well as the radiometer return loss, equivalent noise bandwidth and frequency band are shown in Table I.

The return losses in all connecting network ports and in the radiometer and loads terminals had return losses on the order of 25 dB. This allowed us to ignore the reflections from the connecting network uncertainty analysis and use the simplified conversion (Eq. (20)). Note, however, reflections do have an affect on the nominal brightness temperature conversions. Then the network uncertainty analysis is reduced to a similar situation as with the Heatable load. Equations (15) and (16) with new symbols are repeated here

$$T_{OUT} = T_{RL}10^{-L/10} + (1-10^{-L/10})T_0 \qquad (22)$$

where T_{RL} is the RJ temperature of one of our calibration loads and T_0 is the RJ temperature of the lossy connecting network and L is its loss in dB. The uncertainty ΔT_{OUT} is obtained by differentiating Eq. (22) with respect to L, T_{RL} and T_0 resulting in

$$\Delta T_{OUT} = 0.23g(T_0 - T_{RL})\Delta L + g\Delta T_{RL} + (1-g)\Delta T_0 \qquad (23)$$

where $g = 10^{-L/10}$. The first term describes the error in the connecting network loss measurement. The uncertainty ΔL was determined through a series of measurements. We measured waveguide components with known attenuation with several network analyzers. These measurements differed negligibly when the equivalent noise bandwidth of the radiometer is considered and only a small residual error remained due to a reactive ripple. This measurement artefact slightly increased the measurement uncertainty. We attributed uniformly distributed uncertainties of ±0.36 K and ± 0.07 K for the Cryogenic load and Heatable load respectively for this loss term.

TABLE II. TYPICAL CALIBRATION LOAD BRIGHTNESS TEMPERATURES AND THEIR UNCERTAINTIES AT THE LOAD TERMINALS AND AT THE CALIBRATION PLANE.

	Typical T_B [K]		Uncertainty [K]	
Calibration Load	@Load	@Cal plane	@Load	@Cal plane
Cryogenic load	83[1]	110[4]	± 1.25	± 1.23
Ambient temperature load	300[2]	300	± 0.30	± 0.30
Heatable load	346[3]	342[4]	± 0.29	± 0.30

1: Depends on atmospheric pressure and ambient temperature of the laboratory.
2: Depends on the set temperature of the radiometer box which is 28C for the presented value.
3: Depends on the set temperature of the matched load and on the laboratory ambient temperature. The set temperature is 80C for the presented value.
4: Depends on the set temperature of the Connecting network and its scattering parameters. The set temperature is 28C for the presented value.

The second term presents the calibration load uncertainty and the third term the uncertainty resulting from the connecting network physical temperature measurement. Since there the loss L is close to 0 dB and thus g $\approx$ 1, the third term is clearly smaller than the second. The final Cryogenic load brightness temperature uncertainty approaches a normal distribution due to its many unrelated uncertainty sources. The physical temperature measurement uncertainty is assumed to be uniformly distributed. The Heatable load uncertainty is dominated by the underlying physical temperature measurement. Therefore its distribution resembles uniform distribution. To combine all three uncertainty sources in the Cryogenic load and Heatable load Forward Conversion we used a MCS.

The uncertainty distributions of each load, as previously mentioned, have different shapes. To allow comparison between the loads we report 99% confidence interval estimate obtained from the MCS for each load at the load terminal and at the calibration plane. We repeated the computations 10^6 times for unvarying confidence interval estimates. These uncertainties are summarized in Table II. Each frequency point in the measurements was individually Forward Converted before averaging over the radiometer equivalent noise bandwidth to the single value presented in the table.

It might seem surprising that the uncertainty in the Cryogenic load is smaller at the calibration plane than at the load terminal. The reason is simply due to the loss factor g in the Eq. (23). It has a value between zero and one. This replaces some of the uncertainty of the Cryogenic load in the second term to a smaller uncertainty of the third term.

The Ambient load analysis is simple. Our radiometer is enclosed in a thermally insulated and temperature stabilized radiometer box. The box also holds the Ambient temperature load and the connecting network. Therefore the Ambient temperature load brightness temperature T_{AL}, the connecting network RJ temperature T_0 and the brightness temperature of the radiometer reverse noise feed T_R are nearly the same. This makes the converted brightness temperature T_{OUT} practically insensitive to the losses and reflections of the connecting network as can be observed from Eq. (17).

D. Brightness Temperature Uncertainties at the Scene Terminals

Before the Reverse conversion, the measured scene brightness temperature at the calibration plane needs to solved with a calibrated radiometer. For each measured load the radiometer output voltage U is related to the brightness temperature T at the input by $U_x = GT_x + U_0$ where x is a particular load connected to the radiometer input. G and U_0 are the radiometer gain and offset respectively. Two measurements with known calibration loads are required to solve these unknowns. After the unknowns are solved they can be used to determine the scene brightness temperature. If there are uncertainties in the calibration load nominal temperatures, these lead to an uncertainty in the scene brightness temperature. ΔT is defined as the difference between the measured and the true value. Using the above relation between radiometer output voltage and the input brightness temperature with two calibration loads, G and U_0 can be solved for. After these are determined they can be used again with the voltage brightness temperature relation of the scene measurement to determine a first order approximate relation for the solved scene brightness temperature uncertainty at the calibration plane as

$$\Delta T^S_{OUT} = \frac{T_{cold}-T_{OUT}}{T_{hot}-T_{cold}}\Delta T_{hot} - \frac{T_{hot}-T_{OUT}}{T_{hot}-T_{cold}}\Delta T_{cold} \quad (24)$$

where T_{cold} and T_{hot} refer to two calibrations loads (cold and hot) in general and ΔT_{cold} and ΔT_{hot} are their uncertainties. From this equation it is easily seen that the uncertainty of the calibration loads are multiplied by factors that depend on the nominal brightness temperatures of both calibration loads and the scene. A small separation of calibration load brightness temperatures increase the error. Having calibration load brightness temperatures far from the scene brightness temperature also magnifies the uncertainty of the calibration loads. It also shows the importance of accurate cryogenic loads when cold scenes are measured.

The final step in the analysis is to solve for the scene brightness temperature and its uncertainty with the Reverse conversion. The Reverse conversion can be made with Eq. (21). The uncertainty analysis can be directly adapted from that of the Forward Conversion. For the same reasons as described for the Forward Conversion apply and a simplified version of the Reverse conversion can be used for the uncertainty analysis. Assuming no reflections Eq. (21) reduces to

$$T_{RL} = \frac{T_{OUT} - (1-g)T_0}{g} \quad (25)$$

where symbols have the same meaning as before. By differentiating the above equation with respect to L, T_{OUT} and T_0 we obtain the final scene uncertainty ΔT^S_{RL}

$$\Delta T^S_{RL} = \frac{0.23(T_{OUT}-T_0)}{g}\Delta L + \frac{1}{g}\Delta T^S_{OUT} - \frac{1-g}{g}\Delta T_0 \quad (26)$$

This is the final step in obtaining the uncertainty of scene brightness temperature. The uncertainty contribution of this conversion is comparable to that of Forward Conversion except that the term ΔT^S_{OUT} can easily dominate the final scene brightness temperature uncertainty.

VII. Experimental Verification

A. Verification of the Cryogenic Load Brightness Temperature

Two of our three calibration loads that we discussed are based on a high precision matched load (the Ambient temperature load and Heatable load) whose physical temperatures we monitor with a platinum temperature sensor. The uncertainty of these calibration loads is dominated by the underlying physical temperature measurement. We used a worst case uncertainty of ± 0.3 K for this temperature. Therefore we are quite confident that the uncertainty in our model for these two loads is valid. For the same reasons we believe that the uncertainty related to the connecting network is also valid. We calibrated our radiometer using the Ambient temperature load and the Heatable load and measured the Cryogenic load brightness temperature at the calibration plane. The uncertainty in the Ambient temperature load and Heatable load brightness temperatures lead to an error in the solved brightness temperature of the T_{CL}. Using the uncertainties for the Ambient temperature load and the Heatable load listed in Table II we obtained maximum deviation of ± 3.0 K for the measured T_{CL}. This clearly weakens our ability to measure accurately and with certainty our Cryogenic load brightness temperature. However, our analysis deals with worst case scenario and the measured nominal value is more probable than the extremes. We make the comparison between measured nominal values and the model and acknowledge the limitation in our verification measurement.

A period of 97 h of measured Cryogenic load brightness temperature solved at the calibration plane is shown in Fig. 6. Within this period the Cryogenic load was cooled down five times. The usual cool down time was about five hours. Each cool down has on average 15 cyclic observations of each three loads. Each cycle is used to calibrate the radiometer and solve the brightness temperature of the Cryogenic load i.e. each cooldown produces on average 15 solved Cryogenic load brightness temperatures. This is the noisy curve (blue) in Fig. 6 where the mean brightness temperature of each cool down is indicated with a circle. The standard deviations of the means are shown which present the characteristic noise of the radiometric measurements. The uncertainty in the Cryogenic load model shown in the Fig. 6 is the propagated uncertainty at the calibration plane which we gave in Table II.

The model prediction and solved brightness temperature are in good agreement. The average difference between the model estimates and measured brightness temperatures over the total measurements period is 0.37 K for the Cryogenic load. This is clearly well within our predicted load uncertainty limits.

B. Verification of the Cryogenic Load Stability

The stability of the Ambient temperature load and the Heatable load mainly depends on the stability of the temperature controller. The stability is directly determined by continuously measuring the physical temperatures of the matched loads and the waveguides connecting the loads to the radiometer. The platinum sensor used has less than 0.1 K drift in a month. Therefore even if the loads were to drift small amounts, it is known. The Cryogenic load stability, however, can not be simply guaranteed by measuring the atmospheric pressure and physical temperatures which are the model input parameters. The model is a complex set of many factors and to achieve certainty that our load truly is stable, a verification measurement was performed.

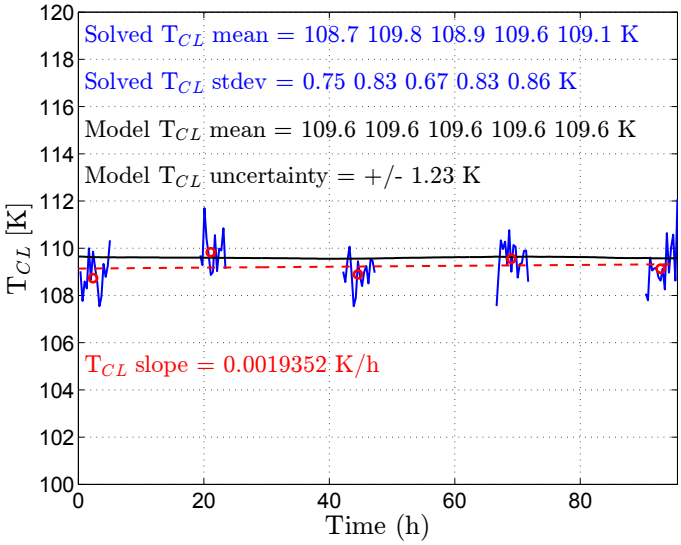

Fig. 6. Measured (solid blue) and its linear fit (dashed red) compared to the modeled (solid black) Cryogenic load brightness temperature during the cool-downs. The values are given in the calibration plane.

The presented Cryogenic load brightness temperature measurement (described in previous section) can be used to analyze load stabilities. The brightness temperature of the unknown load in this measurement (CL) is well below the brightness temperatures of the known calibration loads (AL and HL). Therefore the solved brightness temperature data are noisy as shown in Fig. 6. The linear fit that reveals the drift rate is therefore not reliable. We analyzed the effect of measurement noise to the obtained drift rate via MCS. We assumed that our load is stable and has no drift. We then used the measured standard deviation of each cooldown (shown in Fig. 6) and generated randomly the same amount of cooldown measurements and assigned each a random value from a normal distribution with the same standard deviation as measured. This was repeated 10000 times and the calculated standard deviation of the slope revealed that our Cryogenic load is fully stable within our measurement accuracy. The simulated standard deviation of the slope was 0.00288 K/h which is the same order of magnitude as the measured slope value of 0.00194 K/h. The measurement indicates that our Cryogenic load is stable within our measurement accuracy and that it is suitable for long term stability measurements.

VIII. Conclusion

We presented a radiometer calibration load uncertainty analysis. We described how the uncertainty in such loads can be analyzed and how the uncertainties propagate to the scene brightness temperature measurement. Our analysis included the design of three radiometer calibration loads and a method

for calculating their nominal brightness temperatures and their corresponding uncertainties. The nominal temperatures for the Cryogenic load, the Ambient temperature load and for the Heatable load were 83 K, 300 K and 346 K, respectively. The uncertainties found for the three loads were ± 1.25 K, ± 0.30 K and ± 0.30 K. The main source of uncertainty for the Cryogenic load as well as for the increase in the nominal brightness temperature, was the waveguide section of the horn antenna. The main source of uncertainty for the other two loads was the uncertainty of the temperature sensor used to monitor the termination of the loads. All of our loads are fairly simple to construct and are scalable to frequencies where waveguides are convenient to use. However, the uncertainty analysis principles scale beyond that of waveguide structures. Guidelines how to further improve the calibration loads and minimize the effect of the connecting network and thus the overall radiometric measurement performance, were also discussed. The effect how the nominal brightness temperatures can magnify the load uncertainties was also addressed and it was found that without proper engineering even small uncertainty in the calibration load brightness temperature can be significant if calibration load brightness temperatures are close to each other and/or far from the scene brightness temperature.

ACKNOWLEDGMENT

This study was done within the ESA project Calibration Loads for Radiometers. The authors would like to thank DA-Design Oy for the possibility of participating in this interesting project and for the support in preparing this publication. Our project partners ESA (Petri Piironen), IAF Fraunhofer (Ernst Weissbrodt, Markus Rösch) and VTT/MilliLab (Mikko Kantanen, Jussi Varis) deserve our thanks for fruitful co-operation.

REFERENCES

[1] C. L. Trembath, D. Wait, G. Engen, and W. Foote, "A low-temperature microwave noise standard," *IEEE Transactions on Microwave Theory and Techniques*, vol. 16, no. 9, pp. 709–714, Sep 1968.

[2] W. N. Hardy, "Precision temperature reference for microwave radiometry," *IEEE Transactions on Microwave Theory and Techniques*, vol. 21, no. 3, pp. 149–150, Mar 1973.

[3] W. C. Daywitt, "Design and error analysis for the WR10 thermal noise standard," National Bureau of Standards, Dec 1983.

[4] T. Hewison and A. McGrath, "Performance assessment of liquid nitrogen calibration target supplied by fred solheim (radiometrics) at 89, 157 and 183GHz," MRF Technical Note 39, Jun 2001.

[5] J. D. Kraus, *Radio Astronomy 2nd ed.* Cygnus-Quasar Books, 1986.

[6] W. C. Daywitt, "A coaxial noise standard for the 1 GHz to 12.4 GHz frequency range," National Bureau of Standards, Mar 1984.

[7] B. Pospichal, G. Maschwitz, N. Kuchler, and T. Rose, "Standing wave patterns at liquid nitrogen calibration of microwave radiometers," in *9th International Symposium on Tropospheric Profiling, P35*, 2012.

[8] C. T. Stelzried, "Microwave thermal noise standards," *IEEE Transactions on Microwave Theory and Techniques*, vol. 16, no. 9, pp. 646–655, Sep 1968.

[9] G. Maschwitz, U. Lhnert, S. Crewell, T. Rose, and D. Turner, "Investigation of ground-based microwave radiometer calibration techniques at 530 hpa," *Atmospheric Measurement Techniques*, vol. 6, no. 10, pp. 2641–2658, Jan 2013.

[10] G. Zhao, M. ter Mors, T. Wenckebach, and P. C. M. Planken, "Terahertz dielectric properties of polystyrene foam," *J. Opt. Soc. Am. B*, vol. 19, no. 6, pp. 1476–1479, Jun 2002.

[11] J. Sanford, "A luneberg-lens update," *IEEE Antennas and Propagation Magazine*, vol. 37, no. 1, pp. 76–79, Feb 1995.

[12] F. T. Ulaby, R. K. Moore, and A. K. Fung, *Microwave Remote Sensing Volume 1*. Norwood: Artech House, 1981.

[13] J. Randa, D. Walker, A. Cox, and R. Billinger, "Errors resulting from the reflectivity of calibration targets," *IEEE Transactions on Geoscience and Remote Sensing*, vol. 43, no. 1, pp. 50–58, Jan 2005.

[14] G. De Amici, R. Layton, S. Brown, and D. Kunkee, "Stabilization of the brightness temperature of a calibration warm load for spaceborne microwave radiometers," *IEEE Transactions on Geoscience and Remote Sensing*, vol. 45, no. 7, pp. 1921–1927, Jul 2007.

[15] D. M. Pozar, *Microwave Engineering 3rd ed.* John Wiley & Sons, 2005.

Matti Kaisti received his B.Sc. in electrical engineering from Turku University of Applied Sciences in 2008 and his M.Sc. degree in 2012 from University of Turku, both in electrical engineering.

From 2008 to 2012 he worked as an RF design engineer in DA-Design OY in Finland. During this time he was involved in developing high voltage pulse modulators for weather radars and radar transmitters for detection of oil from sea surface. In ESA research project, Calibration Loads for Radiometers, he was involved in developing total power radiometer systems for Ka-, V- and W-band. This paper is based on this work.

Currently he is working towards the Ph.D. degree in electronics in University of Turku.

Miikka Altti received his M.Sc. degree in Communication Circuits from Tampere University of Technology, Tampere, Finland in 2008. He has been working as an RF Design Engineer in DA-Design Oy, Jokioinen, Finland since 2009.

Miikka Altti has been involved in European Space Agency (ESA) space projects, like development of C-band Transmit Gain Unit (TGU), part of SAR subsystem, for ESA Sentinel 1-A and 1-B satellites.

In ESA research project, Calibration Loads for Radiometers, Miikka Altti was involved in development of Ka-, V- and W-band total power radiometers and carried out the radiometric characterizations of Active Calibration Sub-Systems (ACSSs) including Active Cold Load MMICs. This paper is based on this work.

Currently he is involved in development of X-band Switch Matrix, part of new generation SAR, for future space missions.

Torsti Poutanen received his M.Sc. degree in Technical Physics at Helsinki University of Technology (now Aalto University) in 1983 and Ph.D. degree in Theoretical Physics at University of Helsinki in 2005. From 1983 to 2002 he worked in the R&D of the telecom industry in Finland developing radio communications and wireless modem circuits, algorithms and devices. From 2002 to 2010 he worked in the data analysis of ESA Planck project. Planck satellite made a full sky survey of cosmic microwave background radiation.

From 2010 to 2013 Torsti Poutanen worked in DA-Design Oy in Finland. During that time he worked in an ESA project whose title was Calibration Loads for Radiometers. This paper is based on this work.

Currently Torsti Poutanen works in Elektrobit Wireless Communications Ltd in Finland, where he works with wireless communications products and networks for public safety and military purposes.